Modeling, Analysis, and Optimization of Omega-Shaped Magnetic Field Energy Harvester for Self-Powered Three-Core Cable Sensors

Yonghong Zhou, Yong Li, *Senior Member, IEEE*, Shunpan Liu, *Senior Member, IEEE*, Jiefeng Hu, *Senior Member, IEEE*, and Zhengyou He, *Senior Member, IEEE*

***Abstract*—In nonuniform magnetic field environments around three-core power cables, conventional magnetic field energy harvesters (MFEHs) typically suffer from low power density due to the mutual cancellation of three-phase magnetic fluxes. To address this limitation, this article proposes an OS-MFEH based on the amplitude and phase characteristics of the surrounding magnetic flux density. The proposed structure enhances the induced voltage and mitigates output degradation caused by flux cancellation, while also reducing demagnetization effects. A mathematical model of the harvester's output power is developed, incorporating the influence of the magnetic field generated by the harvester coil. Guided by this model, the core dimensions and material properties are systematically optimized to achieve improved performance. The resulting design not only achieves improved power density but also prevents magnetic core saturation—an issue commonly overlooked when coil-induced magnetic fields are neglected. The experiment verified the effectiveness of proposed omega-shaped MFEH structure and the optimization method. The experimental prototype volume is 45.8 cm^3 and can achieve an output power of 12.86 mW to 84.2 mW within 100 A_{RMS} to 250 A_{RMS}. Within a three-phase current imbalance of 10% , OS-MFEH can still supply power to the load.**

***Index Terms*—Magnetic field energy harvester (MFEH), parameter optimization, power density, self-powered, three-core cable.**

I. Introduction

ONLINE monitoring and intelligent diagnosis of operational status of cables and cable joints are essential support for building a highly reliable smart grid [1], [2]. However, wireless sensor networks that obtain device critical information are constrained by the coverage range of wired power supply and bottleneck of battery maintenance costs. This problem results in poor power supply continuity and reliability for sensors. Fortunately, magnetic field energy harvesters (MFEHs) utilize the persistent magnetic field around cables to overcome limitations of solar, wind, and vibration energy harvesting in cable trenches. They provide a stable and reliable wireless power supply solution for monitoring sensors. Nowadays, MFEHs can be divided into cable-clamped magnetic field energy harvesters (CCMFEHs) [3], [4], [5] and free-standing magnetic field energy harvesters (FSMFEHs) [6], [7], [8], [9], [10]. With watt-level output power, CCMFEHs can effectively power high-power monitoring devices. However, they must be clamped onto power lines and have a relatively large volume. In contrast, FSMFEHs can be flexibly deployed in any space with alternating magnetic fields, significantly improving installation flexibility.

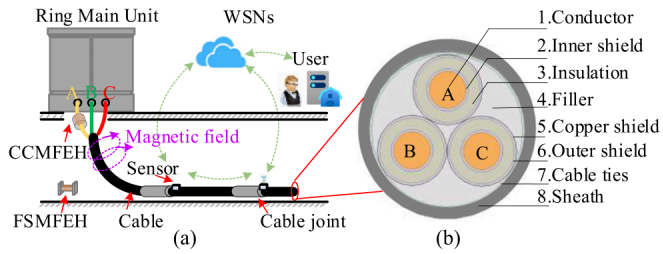

Fig. 1. Diagram of (a) online monitoring for self-powered sensors in three-core cable scenario based on MFEH, and (b) three-core cable.

Existing research on MFEHs focuses on single-phase conductors, such as overhead lines [3], busbars [8], power cables [9], HVDC transmission lines [11]. In fact, three-core cables account for a significant proportion of power system failures. Survey data [12] shows 75% of power distribution system failures originate from cable faults, with three-core cables being the predominant source. Due to complex structures and construction-induced defects, the cable joints have a higher failure rate compared to the cable bodies themselves. This makes the requirement of reliable self-powered sensors particularly prominent, as shown in Fig. 1. Unfortunately, traditional CCMFEH is difficult to migrate directly from single-phase to three-phase scenario, primarily due to mutual cancellation of three-phase magnetic flux. To harvest energy from a three-core cable, a harvester is proposed with a toroidal core and three-section coils [13], [14]. Since three sections of coils are wound on the same toroidal magnetic core,

Received 25 August 2025; revised 7 November 2025; accepted 4 December 2025. Date of publication 11 December 2025; date of current version 25 February 2026. This work was supported by Sichuan Science and Technology Program under Grant 2024NSFJQ0011. Recommended for publication by Associate Editor A. Kuperman. *(Corresponding author: Yong Li.)*

Yonghong Zhou, Yong Li, Shunpan Liu, and Zhengyou He are with the Key Laboratory of Magnetic Suspension Technology and Maglev Vehicle, Ministry of Education, School of Electrical Engineering, Southwest Jiaotong University, Chengdu 610031, China (e-mail: yonghong_zhou@my.swjtu.edu.cn; yong_li@swjtu.edu.cn; liusp@my.swjtu.edu.cn; hezy@swjtu.edu.cn).

Jiefeng Hu is with the Centre for New Energy Transition Research, Federation University Australia, Mount Helen, VIC 3353, Australia (e-mail: j.hu@federation.edu.au).

Color versions of one or more figures in this article are available at https://doi.org/10.1109/TPEL.2025.3643429.

Digital Object Identifier 10.1109/TPEL.2025.3643429

the three-phase magnetic fields will still overlap and weaken each other, resulting in a low effective magnetic flux. Based on the characteristics of the rotating magnetic field in a three-core cable, Yan et al. [15] innovatively proposes a 3-slot/3-tooth core structure similar to that of an induction motor. This design enhances coupling between the core and the three-phase rotating magnetic field. Compared to the aforementioned designs, this core achieves significantly higher magnetic flux with the same volume. However, due to the inherent limitation of three-phase magnetic flux mutual cancellation in a closed core, the final 465 cm^3 prototype in [15] delivers only ~2 mW at 50 A_{RMS}.

In contrast, FSMFEHs are promising because they feature a nonclosed magnetic core, which enhances asymmetric coupling between the coil and one of the phases in a three-phase cable. For instance, the toroidal core can be segmented into three split parts while retaining a three-segment coil configuration [16]. This approach reduces the cancellation effect of induced voltages through coil design and magnetic circuit decoupling, but the ability to utilize the strong magnetic field on the cable surface is still limited. Additionally, this core with a low length-to-diameter ratio exhibits strong demagnetization effects [7]. To enhance the ability of collecting cable surface magnetic field, a notched ring core is proposed in [17]. The optimal notch position is determined by identifying the maximum gradient points of magnetic flux variation rate along the cable surface. Regrettably, Liu et al. [17] only concludes that notch core should be connected to 60° positions left and right of one phase conductor. Meanwhile, absence of theoretical guidance hinders power density improvement. Additionally, the space utilization of the notched ring core is low. In conclusion, the mutual cancellation of three-phase magnetic fields mentioned in the above works remains unresolved, and the demagnetizing effect inherent in nonclosed cores further increases energy harvesting difficulty. Furthermore, without the guidance of mathematical models, even if the overall structure of core and coil is proposed, it is difficult to effectively analyze and quantify the impact of system parameters on output power density.

Through theoretical modeling, researchers incorporate demagnetization effects and provide optimization methods for FSMFEH parameters under single magnetic field source scenarios [8], [9], [10], [11]. However, a key limitation is that the modeling process ignores the influence of coil current and load on the magnetization state of the core, which may lead to an incorrect evaluation of the core saturation state. Notably, in the three-core cable case, due to the complexity of magnetic field superposition and the difficulty of quantifying core parameters, the modeling method cannot be directly transferred from a single-conductor case. The above factors lead to a lack of mathematical model for characterizing the magnetoelectric coupling relationship between the parameters of FSMFEH and the output power. The absence of this critical model severely limits further improvements in the power density of FSMFEH.

To address the challenges above, this article proposes a novel FSMFEH structure and establishes an accurate magnetoelectric conversion model for optimizing design. The key innovations and contributions are summarized as follows:

1) A detailed analysis of magnetic field distribution patterns of three-core cable is conducted. An OS-MFEH is proposed to enhance the coupling between the coil and the target conductor while effectively reducing the impact of three-phase magnetic field superposition weakening. Meanwhile, low demagnetization effects can also be achieved by adopting a length-to-diameter ratio design.
2) The comprehensive influence of coil current and load on the magnetization state of the magnetic Core is revealed. A full-parameter output power model is established for the proposed OS-MFEH. Based on theoretical models, the core and coil parameters of the proposed OS-MFEH are synergistically optimized to improve power density and avoid core saturation. The impact of three-phase unbalanced currents on the output of OS-MFEH is also analyzed.

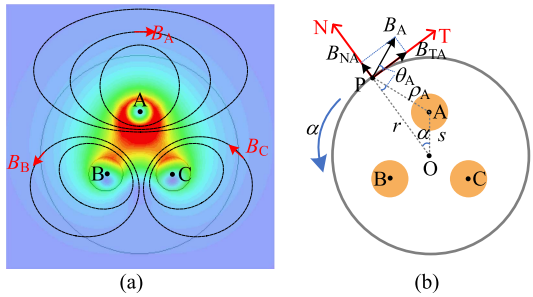

Fig. 2. (a) Magnetic field simulation result of a three-core cable at $t = 5$ ms ($i_A = 141.4$ A, $i_B = i_C = 70.7$ A). (b) Schematic diagram of the 2D decomposition of normal magnetic flux density and tangential magnetic flux density.

II. Omega-shaped MFEH for Three-Core Cable

A. Surface Magnetic Field Distribution of Three-Core Cable

The characteristics of the magnetic field distribution are the primary prerequisite for guiding the design of the core structure. Ideally, the cable carries a balanced three-phase current. The simulation result for the magnetic field distribution with a three-phase current RMS value of 100 A is shown in Fig. 2(a). The cable surface field shows a nonuniform spatial distribution due to conductor current interactions and geometric arrangement. For subsequent analysis, magnetic flux density B_j ($j = A, B, C$) on the cable surface is decomposed into two components. One part is the tangential component B_T, which is tangent to the cable surface. The other part is the normal component B_N, which is perpendicular to the cable surface. The 2D decomposition schematic of each component is shown in Fig. 2(b). In this article, taking the 8.7/10 kV YJV-3 × 95 mm^2 three-core cable as an example. The relative permeability of each insulation layer in nonarmored cables is nearly 1, thus exerting minimal influence on magnetic field distribution [17], [22].

Based on the Biot–Savart law, B_T and B_N, which are generated by three-phase currents, can be expressed as

$$\begin{cases} B_T(\alpha,t) = B_{TA}(\alpha,t) + B_{TB}(\alpha,t) + B_{TC}(\alpha,t) \\ \qquad\quad = \sum \frac{\mu_0 i_j(t)}{2\pi\rho_j} \cos(\theta_j), (j = A,B,C) \\ B_N(\alpha,t) = B_{NA}(\alpha,t) + B_{NB}(\alpha,t) + B_{NC}(\alpha,t) \\ \qquad\quad = \sum \frac{\mu_0 i_j(t)}{2\pi\rho_j} \sin(\theta_j), (j = A,B,C) \end{cases} \tag{1}$$

TABLE I
VARIABLES IN THE EQUATION (1)

j	A	B	C
$i_j(t)$	$\sqrt{2}I_p\sin(\omega t)$	$\sqrt{2}I_p\sin(\omega t-\frac{2\pi}{3})$	$\sqrt{2}I_p\sin(\omega t-\frac{4\pi}{3})$
$\cos(\theta_j)$	$[r-s\cos(\alpha)]/\rho_A$	$\left[r-s\cos(\alpha-\frac{2\pi}{3})\right]/\rho_B$	$\left[r-s\cos(\alpha-\frac{4\pi}{3})\right]/\rho_C$
$\sin(\theta_j)$	$s\sin(\alpha)/\rho_A$	$s\sin(\alpha-\frac{2\pi}{3})/\rho_B$	$s\sin(\alpha-\frac{4\pi}{3})/\rho_C$
ρ_j	$\sqrt{r^2+s^2-2rs\cos(\alpha)}$	$\sqrt{r^2+s^2-2rs\cos(\alpha-\frac{2\pi}{3})}$	$\sqrt{r^2+s^2-2rs\cos(\alpha-\frac{4\pi}{3})}$

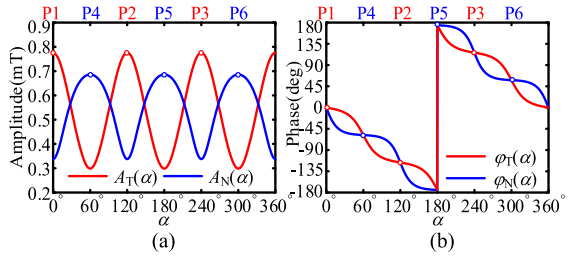

Fig. 3. (a) Amplitude and (b) phase distribution calculation results of the magnetic flux density components on a three-core cable surface with $I_p = 100$ A.

where μ_0 is vacuum magnetic permeability. θ_j is the angle between B_j and the tangent direction. ρ_j is the distance from the center of each Phase conductor to the point P.

The elements in (1) can be obtained in Table I. I_P represents the RMS value of three-phase current. $\omega = 2\pi f$ is the angular frequency, $f = 50$ Hz is the frequency of alternating current. r is the outer radius of the cable, and s is the distance between the center of each phase conductor and the center point O of the cable. α is the scanning angle characterizes different locations on the cable surface. Equation(1) can be further expressed as

$$\begin{cases} B_T(\alpha,t) = A_T(\alpha)\cdot\sin\left[\omega t+\varphi_T(\alpha)\right] \\ B_N(\alpha,t) = A_N(\alpha)\cdot\cos\left[\omega t+\varphi_N(\alpha)\right] \end{cases} \tag{2}$$

where $A_T(\alpha)$ and $A_N(\alpha)$ represent the amplitudes of B_T and B_N, respectively, which are determined by (34). Meanwhile, $\varphi_T(\alpha)$ and $\varphi_N(\alpha)$ denote the initial phases of B_T and B_N, which are calculated by (35).

According to (2), (34), and (35), Fig. 3 presents the calculation results of $A_T(\alpha)$, $A_N(\alpha)$, $\varphi_T(\alpha)$ and $\varphi_N(\alpha)$ as a function of α. $A_T(\alpha)$ and $A_N(\alpha)$ show trends of three peaks and three troughs. It is obtained that points of maximum values of B_T are located at P1 ($\alpha = 0°$), P2 ($\alpha = 120°$), P3 ($\alpha = 240°$), and points of minimum values are located at P4 ($\alpha = 60°$), P5 ($\alpha = 180°$), P6 ($\alpha = 300°$). Meanwhile, the extreme point distribution location of B_N is exactly opposite to that of B_T. The phase in Fig. 3(b) is referenced to the 0° phase of $i_A(t)$. Regardless of B_T and B_N, the value of the phase difference between neighboring extreme points is $2\pi/3$. r and s only affect the magnitude of $A_T(\alpha)$ and $A_N(\alpha)$ values, rather than the extreme point location. The distribution of the extreme points is shown in Fig. 4(a). Due to the rotational symmetry of the three-phase conductor, the magnetic field distribution pattern on the cable surface can be divided into three arc regions of equal length (regions A, B, and C). As illustrated in Fig. 4(a), each of these arcs subtends a central angle of $2\pi/3$ radians.

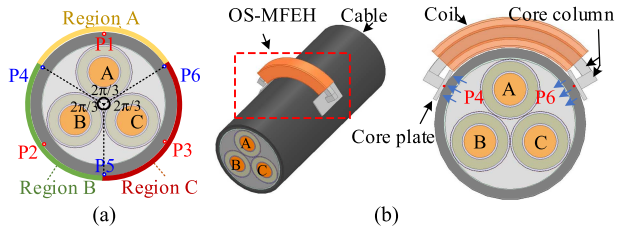

Fig. 4. (a) Schematic diagram of the maximum points of B_T and B_N distributed. (b) Structural details of the OS-MFEH.

B. MFEH Based on Omega-shaped Core Structure

In this article, OS-MFEH is proposed based on the analysis of the amplitude and phase of the magnetic flux density component, as shown in Fig. 4(b). OS-MFEH consists of two core plates, core columns [including a section of arc-shaped core (ASC) column with a round central angle of $2\pi/3$ and two sections of straight columns], and an energy harvesting coil. The core with large ends and slender central, i.e., length-to-diameter ratio, reduces the demagnetization effect and decreases the coil resistance [6], [8]. As shown in Fig. 3, the magnetic field distributions in regions A, B, and C are rotationally equivalent. Thus, the subsequent analysis is carried out with the OS-MFEH placed directly above the Phase A conductor as an example, and the core plates are tangent to P4, P6, respectively.

The proposed core structure enhances the coupling between the coil and the target conductor through three key principles.

1) The core path of the proposed OS-MFEH is highly compatible with the shape of the magnetic field excited by $i_A(t)$, and the coil covers the area with the highest tangential magnetic flux density.
2) Since core plates are tangent to P4 and P6, B_N can enter the magnetic core vertically, minimizing the impact of air gap magnetic resistance, and core plates play a key role as flux collectors.
3) With the OS-MFEH, the magnetic flux path flowing through P4 and P6 is reconstructed. According to the right-hand rule for an ac circuit, the current $i_B(t)$ generates a flux density with zero normal component at point P6. Similarly, $i_C(t)$ has the same effect at point P4. Therefore, the magnetic fields excited by currents $i_B(t)$ and $i_C(t)$ have a limited negative effect on the induced voltage.

To obtain the induced voltage of OS-MFEH, the external magnetic flux density collected by the magnetic core $B_{ex}(t)$ must be calculated. B_N in the region around point P4 (or P6) exhibits high consistency in both amplitude and phase, as shown in Fig. 3. This indicates that the flux density into the core plates is uniform and can be obtained by vector synthesis of B_N at points P4 and P6. Define that the direction from point P4 into the core plate is the positive direction of B_N. The superposition magnetic flux density $B_{ex}(t)$ entering the core from points P4 and P6 can be expressed as

$$B_{ex}(t) = B_N(\alpha_{P4},t) - B_N(\alpha_{P6},t). \tag{3}$$

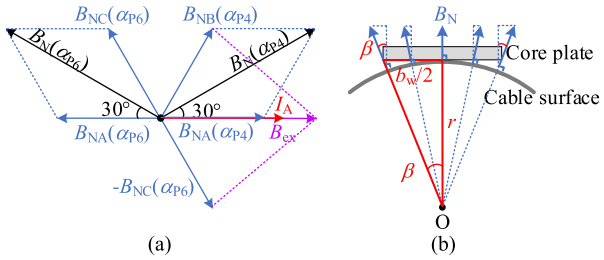

Fig. 5. (a) Schematic diagram of the decomposition of normal magnetic flux density B_N at points P4 and P6. (b) Schematic diagram of normal magnetic flux density B_N entering the core plates.

Here, $B_{ex}(t)$ is related to the amplitude and phase of $B_N(\alpha_{P4},t)$ and $B_N(\alpha_{P6},t)$. Specifically, according to (1), $B_N(\alpha_{P4},t)$ consists of $B_{NA}(\alpha_{P4},t)$, $B_{NB}(\alpha_{P4},t)$, and $B_{NC}(\alpha_{P4},t)$; $B_N(\alpha_{P6},t)$ consists of $B_{NA}(\alpha_{P6},t)$, $B_{NB}(\alpha_{P6},t)$, and $B_{NC}(\alpha_{P6},t)$. According to the right-hand rule, $B_{NC}(\alpha_{P4},t)$ and $B_{NB}(\alpha_{P6},t)$ are nearly zero. Then, taking phase of $i_A(t)$ as a reference, the above vector relationship is shown in Fig. 5(a). Thus, (3) can be further expressed as

$$B_{ex}(t) = B_{NA}(\alpha_{P4},t) + B_{NB}(\alpha_{P4},t) - B_{NC}(\alpha_{P6},t) = \frac{\sqrt{6}s\mu_0 I_P}{2\pi(r^2+s^2-rs)}\sin(\omega t) = \sqrt{2}B_{EX}\sin(\omega t) \quad (4)$$

where B_{EX} denotes the RMS value of $B_{ex}(t)$. $B_{ex}(t)$ remains in phase with $i_A(t)$, which indicates that the magnetic flux inside the core is synchronized with $i_A(t)$. This also proves that the coupling between the coil and Phase A conductor is much stronger than phase B and phase C.

Based on (4), the RMS value U_S of OS-MFEH induced voltage can be expressed as [6]

$$U_S = \omega N \mu_{eff} k_{gap} B_{EX} S_C = \omega N B_m S_C \quad (5)$$

where μ_{eff} is the effective permeability of the core, and N denotes the number of coil turns. S_C is the effective area arc-shaped core column. B_m is the RMS value of the flux density generated by the cable current at the center of the core column. It is worth noting that k_{gap} in (5) is the effective coefficient of B_{EX}. This is due to the presence of two air gaps between the core plates and the cable surface. According to the geometrical relationship in Fig. 5(b), it can be expressed as

$$k_{gap} = \cos(2\beta) = \cos\left[2\arctan\left(\frac{b_w/2}{r}\right)\right] \quad (6)$$

where b_w is the width of the core plates.

C. Equivalent Circuit of OS-MFEH

Fig. 6 shows the equivalent circuit diagram of OS-MFEH with a full-bridge rectifier circuit. Here, u_s is the induced voltage of OS-MFEH, and R_S denotes the resistance of OS-MFEH. The compensation capacitor $C_S = 1/(\omega^2 L_S)$ can eliminate the reactive power loss generated by the coil self-inductance L_S. D_1–D_4 are four rectifier diodes. In Fig. 6(b), the equivalent AC

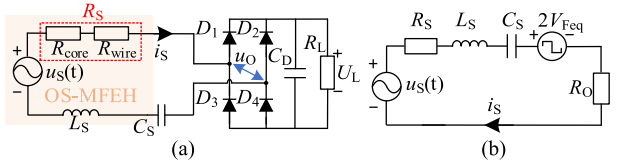

Fig. 6. (a) Equivalent circuit diagram and (b) simplified circuit diagram of the OS-MFEH system.

resistance $R_O = 8R_L/\pi^2$. R_L represents the equivalent load of the sensor.

R_S consists of equivalent core resistance R_{core} and wire resistance R_{wire}. R_{core} reflects the hysteresis loss and eddy current loss in magnetic core. Under low-frequency conditions, the core loss is reduced through the use of high-resistivity soft magnetic materials or laminated fabrication [8], [10]. To achieve a sufficiently high voltage, the number of coil turns is typically increased. Consequently, R_{wire} becomes larger than R_{core}, allowing R_{core} to be neglected.

The equivalent ac voltage drop V_{Feq} of a single diode can be calculated as [19]

$$V_{Feq} = \frac{2\sqrt{2}}{\pi}V_F \approx 0.9V_F \quad (7)$$

where V_F is the dc voltage drop of the diode.

Then, the power P_L obtained by the load can be calculated as

$$P_L = \frac{(U_S - 2V_{Feq})^2}{(R_{wire}+R_{core}+R_O)^2}R_O \approx \frac{(U_S - 1.8V_F)^2}{\left(R_{wire}+\frac{8}{\pi^2}R_L\right)^2}\frac{8}{\pi^2}R_L. \quad (8)$$

In this section, a novel OS-MFEH is proposed, and its basic expressions of the induced voltage and output power are clarified. Nonetheless, the impact of the multiparameter coupling between the core and the coil on the output power remains unknown. The next section will establish a mathematical model for the output power of the OS-MFEH while considering the influence of core and coil parameters.

III. Power Mathematical Model of OS-MFEH

According to (5) and (8), the load power is closely related to the core parameters (μ_{eff}) and coil parameters (R_{wire}, N). μ_{eff} is affected by whether the magnetic core is saturated. This section will quantify each of the above parameters. Meanwhile, clarify the influence of magnetic fields generated by cable current and coil current on the magnetization state of the core.

A. Quantification of Core and Coil Parameters

Due to the demagnetization effect, the effective permeability μ_{eff} of the core can be expressed as [6]

$$\mu_{eff} = \frac{\mu_r}{1 + D_M(\mu_r - 1)} \quad (9)$$

where μ_r is the relative permeability of the core material. D_M ($0 < D_M < 1$) is the demagnetization factor, which is related only to the shape of the core [7]. Thus, optimizing the core parameters and reducing the D_M as much as possible are necessary to

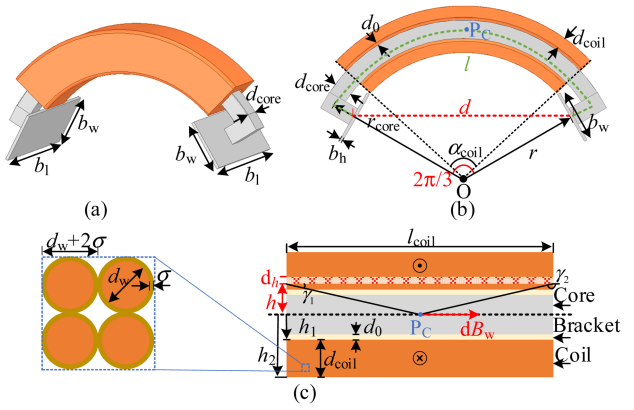

Fig. 7. (a) 3D structure, (b) cross-sectional view, and (c) coil cross-sectional view of OS-MFEH.

improve the μ_{eff}. For long and straight bar-shaped cores, the larger the ratio of length to radius, the smaller the D_M [7].

The proposed core, along with H-shaped core [8], [10] and dumbbell-shaped core [20], features a structure that is larger at both ends and tapers to a slender middle section. To calculate the demagnetization coefficient of the proposed core structure, based on the magnetic flux path length equivalence method described in [8], [10], [20], the proposed core is modeled as a long straight core. The equivalent demagnetization factor $D_{M,\text{eq}}$ can be calculated as

$$D_{M,\text{eq}} = \frac{1.7(0.5K_{\text{eq}})^{0.13}}{g_{\text{eq}}^3}\left(\frac{1}{K_{\text{eq}}}\right)^2 \times \left[ln\left(\frac{1+g_{\text{eq}}}{1-g_{\text{eq}}}\right) - 2g_{\text{eq}}\right] (K_{\text{eq}} > 2) \tag{10}$$

where K_{eq} and g_{eq} are denoted as

$$\begin{cases} K_{\text{eq}} = 2l_{\text{eq}}/d_{\text{core}} \\ g_{\text{eq}} = \sqrt{1-(2/K_{\text{eq}})^2} \end{cases} \tag{11}$$

where l_{eq} is the equivalent magnetic path length. d_{core} is the side length of the core column.

To obtain $D_{M,\text{eq}}$, calculating l_{eq} is the most critical step. The core plates extend the distance between the N-S poles generating the demagnetizing field, thereby reducing the demagnetization coefficient [20]. With the core plates' effect of mitigating demagnetization incorporated into the calculation, l_{eq} is described as

$$l_{\text{eq}} = l_{\text{column}} + \sqrt{{b_{\text{l}}}^2 + {b_w}^2} + 2b_h - d_{\text{core}} \tag{12}$$

where b_{l} and b_h are the length and the thickness of the core plates. l_{column} denotes the effective length of the core column. For the proposed core structure, l_{column} is the distance d between the two ends of the core column rather than the core column length l. The analysis is as follows. l and d are shown in Fig. 7(b). The N-S magnetic poles that generate the demagnetizing field are distributed on the ends of the two core plates [6]. When the core column radius r_{core} varies, l changes accordingly, while d remains fixed under the constraints of B_N maximum value location and cable parameters. Therefore, the distance between the magnetic poles on the core plate remains constant. When other parameters are constant, increasing r_{core}, i.e., extending l, does not reduce $D_{M,\text{eq}}$.

According to the geometric relationship shown in Fig. 7(b), d can be expressed as

$$d = \sqrt{3}(r + b_h). \tag{13}$$

Then, l_{eq} can be further expressed as

$$l_{\text{eq}} = d + 2b_h + \sqrt{{b_{\text{l}}}^2 + {b_w}^2} - d_{\text{core}}. \tag{14}$$

Combining (9), (10), (11), and (14), considering the gain effect of the core plates on the effective permeability, the gain coefficient $\lambda = (l_{\text{eq}}/d)^{1/3}$ [20], the effective permeability $\mu_{\text{eff,eq}}$ of the proposed core can be calculated as

$$\mu_{eff,\text{eq}} = \frac{\lambda\mu_r}{1 + D_{\text{M,eq}}(\mu_r - 1)} = \frac{\mu_r\left[(d + 2b_h + \sqrt{{b_{\text{l}}}^2 + {b_w}^2} - d_{\text{core}})/d\right]^{1/3}}{1 + \frac{1.7(0.5K_{\text{eq}})^{0.13}}{g_{\text{eq}}^3}\left(\frac{1}{K_{\text{eq}}}\right)^2\left[ln\left(\frac{1+g_{\text{eq}}}{1-g_{\text{eq}}}\right) - 2g_{\text{eq}}\right](\mu_r - 1)}. \tag{15}$$

In the case of a fixed core shape, as μ_{r} increases, $\mu_{\text{eff,eq}}$ exhibits a trend of first increasing and then stabilizing [8]. In other words, $\mu_{\text{eff,eq}}$ does not continue to grow as μ_{r} increases. There is a relative magnetic permeability threshold $\mu_{r,\text{th}}$. When $\mu_r > \mu_{r,\text{th}}$, increasing μ_r has a limited effect on $\mu_{\text{eff,eq}}$. To select a suitable core material, it is necessary to obtain $\mu_{r,\text{th}}$. According to (15), when μ_r is sufficiently large, the maximum effective permeability $\mu_{\text{eff,eq\_max}}$ can be expressed as

$$\mu_{eff,\text{eq\_max}} = \lim_{\mu_r \to +\infty} \frac{\lambda\mu_r}{1 + D_{M,\text{eq}}(\mu_r - 1)} = \frac{\lambda}{D_{\text{M,eq}}}. \tag{16}$$

Then, according to (16) $\mu_{r,\text{th}}$ satisfies the following equation:

$$\frac{\lambda\mu_{r,\text{th}}}{1 + D_{M,\text{eq}}(\mu_{r,\text{th}} - 1)} = \xi\frac{\lambda}{D_{M,\text{eq}}} \tag{17}$$

where ξ is defined as the threshold coefficient of effective permeability in this article. Considering μ_r range of commonly used soft magnetic materials (1500 – 100000) [8], [10], take ξ = 0.95. Simplification (17), $\mu_{r,\text{th}}$ is given by

$$\mu_{r,\text{th}} = \frac{\xi}{1-\xi}\left(\frac{1}{D_{M,\text{eq}}} - 1\right). \tag{18}$$

According to (15) and (18), $D_{M,\text{eq}}$ is positively correlated with d_{core}; therefore, a smaller d_{core} results in a larger $\mu_{r\text{·th}}$.

In addition to $\mu_{\text{eff,eq}}$ and $\mu_{r,\text{th}}$, the number of turns N and the resistance R_{wire} of the coil are also critical to the design of OS-MFEH. Depending on the geometry of the coil arrangement in Fig. 7(c), N and R_{wire} can be calculated as

$$\begin{cases} N = \frac{k_P l_{\text{coil}} d_{\text{coil}}}{\pi(d_w/2+\sigma)^2} = \frac{r\alpha_{\text{coil}} d_{\text{coil}}}{(d_w+2\sigma)^2} \\ R_{\text{wire}} = \frac{16r\alpha_{\text{coil}} d_{\text{coil}}\rho(d_{\text{coil}}+2d_0+d_{\text{core}})}{\pi d_w^2(d_w+2\sigma)^2} \end{cases} \tag{19}$$

where d_w and σ are the diameter and insulation thickness of the enamelled wire. σ is about 0.005 mm. k_{p} is the filling factor,

which can be obtained from the turn-to-turn arrangement relationship in Fig. 7(c) as $k_p = \pi/4$. d_0 is the bracket thickness. α_{coil} is the circumferential angle of the coil cross section. According to (24), under the same N, the larger α_{coil}, the smaller R_{wire}. Therefore, α_{coil} is as large as possible within the constraints of the core shape ($\alpha_{\text{coil}} < 2\pi/3$). $\rho = 1.72 \times 10^{-8}$ Ω·m is the resistivity of copper. l_{coil} is the coil cross-section length. d_{coil} is the coil thickness. l_{coil} and d_{coil} can be expressed as

$$\begin{cases} l_{\text{coil}} = r\alpha_{\text{coil}} \\ d_{\text{coil}} = r_{\text{core}} - r - \frac{1}{2}d_{\text{core}} - d_0 - b_h \end{cases}. \tag{20}$$

At this point, $\mu_{\text{eff,eq}}$, N, and R_{wire} have been obtained. Then, substituting (15) and (19) into (5), U_S is expressed as

$$U_S = \frac{\sqrt{3}s\omega\mu_0\mu_{\text{eff,eq}}I_{\text{P}}r\alpha_{\text{coil}}d_{\text{coil}}(4r^2 - b_w^2)d_{\text{core}}^2}{2\pi(4r^2 + b_w^2)(r^2 + s^2 - rs)(d_w + 2\sigma)^2}. \tag{21}$$

Further, substituting (21) and (19) into (8), P_L becomes

$$P_L = \left[\frac{\frac{\sqrt{3}s\omega\mu_0\mu_{\text{eff,eq}}I_{\text{P}}l_{\text{coil}}d_{\text{coil}}(4r^2-b_w^2)d_{\text{core}}^2}{2\pi(4r^2+b_w^2)(r^2+s^2-rs)(d_w+2\sigma)^2} - 1.8V_F}{\frac{16\rho l_{\text{coil}}d_{\text{coil}}(d_{\text{coil}}+2d_0+d_{\text{core}})}{\pi d_w^2(d_w+2\sigma)^2} + \frac{8}{\pi^2}R_L}\right]^2 \frac{8}{\pi^2}R_L. \tag{22}$$

When $R_L = \pi^2 R_{\text{wire}}/8$, the load can obtain maximum power. The total volume of the OS-MFEH coil and core can be expressed as

$$V = \frac{2\pi}{3}r_{\text{core}}[2(d_{\text{coil}} + d_0) + d_{\text{core}}]^2 + 2b_{\text{l}}b_w b_h. \tag{23}$$

The power density D_P of the OS-MFEH is given by

$$D_P = \frac{P_L}{V}. \tag{24}$$

B. Analysis of Magnetic Flux Density Inside the Core Column

The magnetic flux density in the core column is induced by cable current I_P and coil current I_S. In practice, I_S increases monotonically with I_P. Moreover, series resonance of C_S and reduction of R_L also boost I_S. Consequently, the magnetic potential from the coil notably raises the core's magnetic flux density. Once this density reaches the material's saturation point, its relative permeability plummets, severely weakening magnetic coupling and drastically reducing power output. Given the coil's significant influence on the core's magnetization state, this effect must be accounted for in MFEH design to ensure optimal performance.

According to (5), the flux density B_m generated by cable current I_P is calculated by

$$B_m = \mu_{\text{eff,eq}}k_{\text{gap}}B_{\text{EX}} = \frac{\sqrt{3}s\mu_0\mu_{\text{eff,eq}}I_P(4r^2 - b_w^2)}{2\pi(4r^2 + b_w^2)(r^2 + s^2 - rs)}. \tag{25}$$

In order to calculate the flux density generated by I_S, the coil can be simplified as a section of a multilayer densely wound solenoid, as shown in Fig. 7(c). The flux density element dB_W generated by a coil micro element can be expressed as [21]

$$dB_W = \frac{\mu_0\mu_{\text{eff,eq}}J}{2}(\cos\gamma_1 - \cos\gamma_2)\,dh = \mu_0\mu_{\text{eff,eq}}J\cos\gamma_1\,dh \tag{26}$$

where J is the current density of the coil micro element. $\gamma_2 = 180°$ - γ_1, γ_1 is the angle between the coil micro elements and the point P_C in Fig. 7(c). $\cos\gamma_1$ can be expressed as

$$\cos\gamma_1 = \frac{l_{\text{coil}}/2}{\sqrt{(l_{\text{coil}}/2)^2 + h^2}} \tag{27}$$

where h is the height of the coil micro element position.

J can be calculated as

$$J = \frac{NI_S}{l_{\text{coil}}d_{\text{coil}}} = \frac{N(U_S - 1.8V_F)}{l_{\text{coil}}d_{\text{coil}}(R_{wire} + \frac{8}{\pi^2}R_L)}. \tag{28}$$

Furthermore, performing integration on the(26), the flux density B_{W} generated by the N-turn coil can be expressed as

$$\begin{aligned} B_W &= \frac{\mu_0}{2}\mu_{\text{eff,eq}}Jl_{\text{coil}}\int_{h_1}^{h_2}\frac{dh}{\sqrt{(l_{\text{coil}}/2)^2 + h}} \\ &= \frac{\mu_0}{2}\mu_{\text{eff,eq}}Jl_{\text{coil}}\ln\frac{h_2 + \sqrt{h_2^2 + (l_{\text{coil}}/2)^2}}{h_1 + \sqrt{h_1^2 + (l_{\text{coil}}/2)^2}} \end{aligned} \tag{29}$$

where $h_1 = d_{\text{core}}/2 + d_0$ and $h_2 = h_1 + d_{\text{coil}}$.

The phases of B_W and B_m differ by 90° when C_S and L_S are in complete resonance. So, the peak value of the flux density B_{all} can be calculated as

$$B_{\text{all}} = \sqrt{\left(\sqrt{2}B_m\right)^2 + \left(\sqrt{2}B_W\right)^2}. \tag{30}$$

In summary, to ensure that the core possesses a sufficiently high effective permeability and avoids saturation, the selection of core material must satisfy the following requirements:

$$\begin{cases} \mu_r > \mu_{r,\text{th}} \\ B_{\text{sat}} > B_{\text{all,max}} \end{cases} \tag{31}$$

where $B_{\text{all, max}}$ is the maximum flux density inside the core. B_{sat} is the saturation magnetic flux density of the material.

C. Impact of Three-Phase Current Imbalance on OS-MFEH

Due to the three-phase load imbalance, the currents in the cable are not perfectly symmetrical. This imbalance causes OS-MFEH's induced voltage to increase or decrease, which is necessary to analyze its impact on output. The current imbalance factor c is defined by the maximum deviation of a single-phase current from the three-phase average value, with the mathematical expression given as [22]

$$c = \frac{\max|(I_A - I_{\text{av}}), (I_B - I_{\text{av}}), (I_C - I_{\text{av}})|}{I_{\text{av}}} \times 100\% \tag{32}$$

where I_A, I_B, and I_C represent the three-phase currents, respectively. I_{av} is the average value of the three-phase currents.

The induced voltage of the OS-MFEH can be expressed as

$$\begin{aligned} \dot{U}_S &= j\omega\left(M_{\text{A}}I_{\text{A}}\angle 0° + M_BI_B\angle -120° + M_CI_C\angle 120°\right) \\ &= \omega\left(M_AI_A - \frac{1}{2}M_BI_B - \frac{1}{2}M_CI_C\right) \end{aligned}$$

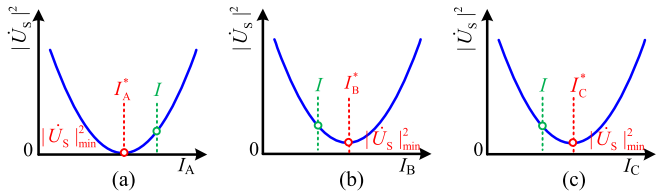

Fig. 8. Relationship between the square of the induced voltage magnitude and the unbalanced current. (a) $I_A \neq I_B = I_C$. (b) $I_B \neq I_A = I_C$. (c) $I_C \neq I_A = I_B$.

$$+ j\frac{\sqrt{3}}{2}\omega(M_C I_C - M_B I_B). \tag{33}$$

where M_A, M_B, and M_C represent the mutual inductance between the coil and the three-phase conductors, respectively.

Equation (33) indicates that the induced voltage is a three-variable function of I_A, I_B, and I_C. Three-phase current imbalance can be categorized into the following two cases. Case 1: Two phases balanced, one phase unbalanced; Case 2: All three phases unbalanced.

Case 1: This case encompasses three classifications: 1) $I_A \neq I_B = I_C$; 2) $I_B \neq I_A = I_C$; and 3) $I_C \neq I_A = I_B$. Assuming the balanced current is I. According to (33), the square of the induced voltage magnitude is a quadratic function of the unbalanced current (serving as the independent variable).

When the OS-MFEH is positioned directly above the A-phase conductor, the condition $M_A > M_B = M_C$ is satisfied. According to (33), a schematic diagram showing the variation of the square of the induced voltage magnitude with unbalanced current can be obtained, as depicted in Fig. 8. I_A^* ($m = A, B, C$) is the condition for U_S to take the minimum value. I_m^* is related to M_A, M_B, and M_C, and satisfies: $I_A^* < I$, $I_B^* > I$, and $I_C^* > I$. Since $M_B = M_C$, categories 2) and 3) are identical. Fig. 8 shows that the induced voltage under balanced three-phase current exceeds the minimum voltage observed during any single-phase current imbalance. When $I_A = I \cdot M_B/M_A = I \cdot M_C/M_A$, the minimum value of U_S can be 0 in Fig. 8. This means OS-MFEH will have no output. However, this situation rarely occurs in practice.

Case 2: All three-phase currents are unbalanced, i.e., $I_A \neq I_B \neq I_C$. This implies that I_A, I_B, and I_C in (33) are all random variables. Therefore, the induced voltage is zero only when both the real and imaginary parts in (33) are zero. Consequently, the solution to this linear equation system is $(I_A, I_B, I_C) = (z \cdot M_C/M_A, z \cdot M_C/M_B, z)$, where $z \in \mathbf{R}$. It follows that the probability of OS-MFEH having no output remains very low.

Thus far, A power mathematical model considering the magnetic field of the OS-MFEH coil has been established. The impact of three-phase current imbalance on induced voltage is also analyzed. In Section IV, the core and coil parameters are optimized and analyzed based on the mathematical model with the objective of high power density.

IV. Optimization of the Proposed OS-MFEH

Under the constraints of cable size and installation space, OS-MFEH is designed based on the parameters specified in Table II. According to (15), since the thickness b_h of the core plate is much smaller than the distance d between the two ends of the core column. Therefore, increasing b_h will improve $\mu_{\text{eff,eq}}$, but this improvement is limited. b_h is set to 1 mm, which facilitates machining without wasting material. With core plate parameters determined, d_{core} becomes the key structural parameter that affects $\mu_{\text{eff,eq}}$. In addition, d_{core} is closely related to N, R_{wire}, so optimizing d_{core} is crucial to improve the power density. To balance practicality and energy harvesting efficiency, d_{core} can be optimized within a range of 4 mm to 11 mm. Small d_{core} risks core fracture; large d_{core} compromises winding space. d_{core} is inversely proportional to $\mu_{\text{r,th}}$. The maximum value of $\mu_{\text{r,th}}$ is 3028 (@$d_{\text{core}} = 4$ mm).

TABLE II
Design Specific Parameters for OS-MFEH

Symbol	Value	Symbol	Value	Symbol	Value
r(mm)	32	b_l(mm)	40	d_0(mm)	1.5
s(mm)	12.6	b_w(mm)	15	α_{coil}(°)	100
r_{core}(mm)	44	b_h(mm)	1	V(cm^3)	45.8

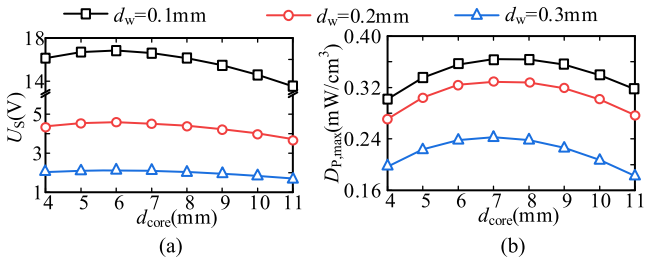

Fig. 9. Calculation results of (a) U_S and (b) $D_{P,max}$ versus d_{core} at different d_w when $I_P = 100$ A.

A. Selection of Core Column Side Length and Wire Diameter

Based on (21), (22) and (24), the coil induced voltage U_S and the maximum power density $D_{P,\max}$ was calculated for different the core column side length d_{core}, as shown in Fig. 9. As d_{core} increases, the effective permeability $\mu_{\text{eff,eq}}$ gradually decreases according to (15), while the magnetic flux area S_C through the coil increases. This leads to an initial increase in U_S, which peaks at $d_{\text{core}} = 6$ mm, as shown in Fig. 9(a). With further increases in d_{core}, the number of coil turns N decreases rapidly according to (19), causing U_S to decline sharply. For $D_{P,\max}$, its trend aligns with U_S as described by (22) and (24). Additionally, the reduction in N decreases the wire resistance R_{wire}. Due to the differential magnitude of changes in U_S and R_{wire}, $D_{P,\max}$ ultimately achieves its peak at $d_{\text{core}} = 7$ mm in Fig. 9(b).

Furthermore, Fig. 9 illustrates that the value of the optimal d_{core} is independent of d_w. This suggests that d_w can be designed independently after the optimal d_{core} has been determined. The curve that $D_{P,\max}$ against d_w is shown in Fig. 10 under $d_{\text{core}} = 7$ mm condition. The OS-MFEH with $d_w = 0.02$ mm exhibits the highest N value, but this also means that R_{wire} is enormous. When $d_w = 0.5$ mm, R_{wire} is smaller, but the voltage drop due to rectification loss accounts for a higher proportion of the

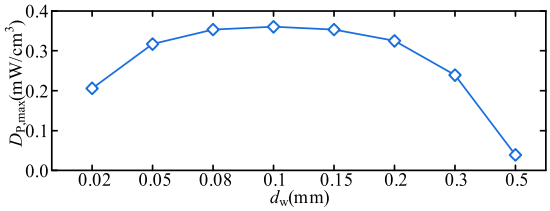

Fig. 10. Calculation results of $D_{\mathrm{P,\ max}}$ versus d_{w} at $d_{\mathrm{core}} = 7$ mm when $I_{\mathrm{P}} = 100$ A.

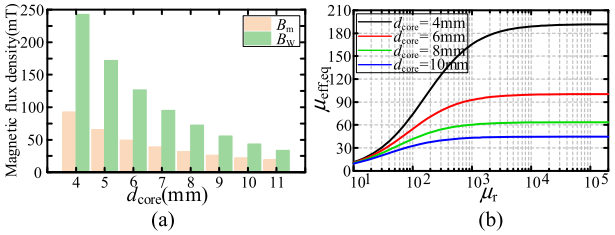

Fig. 11. (a) Calculation results of B_{m} and B_{W} versus d_{core} when $R_{\mathrm{L}} = R_{\mathrm{wire}}\pi^2/8$. (b) $\mu_{\mathrm{eff,eq}}$ versus μ_{r}.

induced voltage. From a practical standpoint, enameled wires with smaller d_w are prone to breakage during winding. With a limited window area, using wires with larger d_w makes it difficult to achieve a high N value. In summary, under these constraints, the optimal $d_w = 0.1$ mm maximizes the power density of the OS-MFEH.

B. Evaluation of Magnetic Density Inside the Core Column

According to (25), (29) and (30), Fig. 11(a) presents a comparison between B_m and B_W across varying d_{core} when $I_P = 100$ A and $d_w = 0.1$ mm. This comparison reveals that B_W is higher than B_m within the entire range of d_{core} variations. The contribution of I_{S} to the core magnetization state is dominant. This also indicates that the magnetic flux density of the coil is the main factor causing eddy current loss in the magnetic core. As the external magnetic field continues to increase, the combined effect of B_W and B_m will saturate the core, causing a significant reduction in μ_r. According to (15), Fig. 11(b) gives the variation of $\mu_{\mathrm{eff,eq}}$ with μ_{r} under different d_{core}. A core with a smaller d_{core} exhibits a higher $\mu_{\mathrm{eff,eq}}$ and thus has stronger magnetic field concentration ability. But this also makes magnetic saturation more likely to occur. When the core d_{core} is smaller, the variation in $\mu_{\mathrm{eff,eq}}$ caused by a change in μ_r is more drastic.

To prevent core saturation, the level of magnetic density inside the core of OS-MFEH under different operating conditions needs to be evaluated. According to (25), (29) and (30), Fig. 12 presents the variation of B_{all} under different I_P and R_L when $d_w = 0.1$ mm. When $d_{\mathrm{core}} = 6$ mm and $I_P = 250$ A, B_m is only 0.17 T, but B_{all} exceeds 0.9 T, which shows that the risk of saturation of the material will be seriously underestimated if the coil magnetic field is ignored. Comparison of Fig. 12(a) and Fig. 12(b), $B_{\mathrm{all,max}}$ decreases significantly from 0.93 T to 0.54 T by 41.94% when d_{core} is increased from 6 mm to 8 mm. According to Fig. 9(b), although $D_{P,\mathrm{max}}$ varies by less than

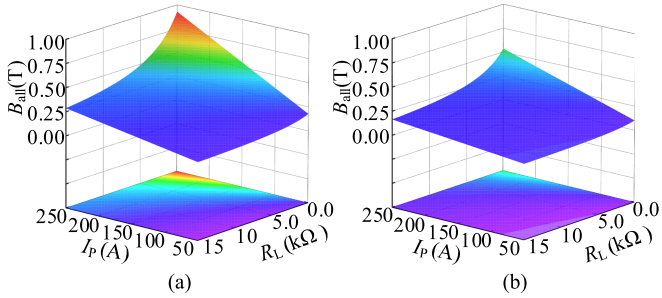

Fig. 12. Calculation results of B_{all} under different I_{P} and R_{L}. (a) $d_{\mathrm{core}} = 6$ mm, $N = 30000$. (b) $d_{\mathrm{core}} = 8$ mm, $N = 25300$.

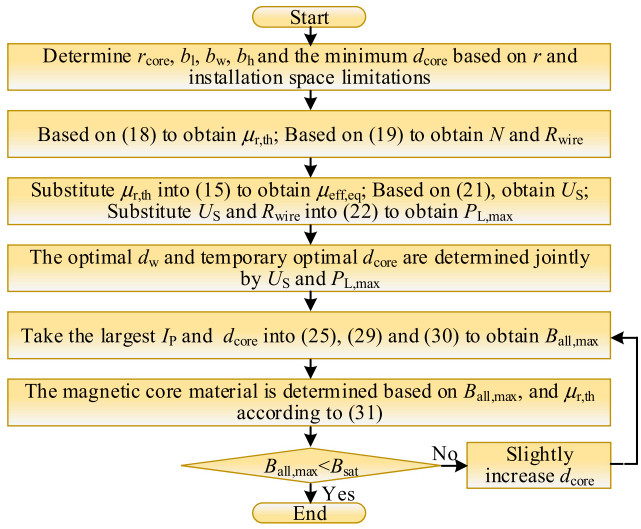

Fig. 13. Optimization procedure for the OS-MFEH.

2% when d_{core} is in the range of 6 to 8 mm, OS-MFEH with the smaller d_{core} requires the selection of materials with higher saturation flux density. Thus, increasing d_{core} is a simple and effective measure to prevent core saturation when B_{sat} of the core material is smaller than $B_{\mathrm{all,\ max}}$.

Ultimately, μ_{r} and B_{sat} must satisfy (31) when selecting core material. In summary, the optimized design process for OS-MFEH is shown in Fig. 13.

V. Simulation and Experimental Verification

A. Simulation Verification

To verify the validity of the magnetic coupling performance of the proposed core structure, three core structures—toroidal-shaped core (TSC), ASC, and omega-shaped core (OSC) —were modeled in ANSYS Maxwell 3D (Version 19.2) using the Eddy current solver, as shown in Fig. 14. Fig. 15 shows the variation of the magnetic flux through different core cross sections (S1, S2). TSC possesses a high permeability due to the absence of demagnetizing effect. Therefore, the three-phase magnetic fluxes are enhanced. However, since the three-phase magnetic fluxes mutually weaken each other, the superposed flux is small. In other words, the closed magnetic core amplifies the weakening

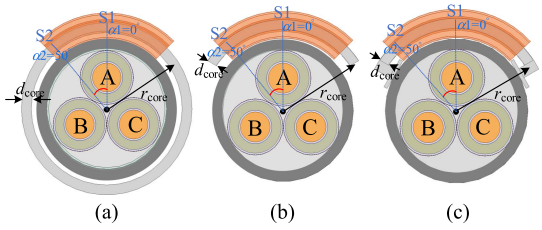

Fig. 14. $r_{core} = 44$ mm, $d_{core} = 6$ mm, three types of core structures simulation model. (a) Toroidal-shaped core. (b) Arc-shaped core. (c) Omega-shaped core.

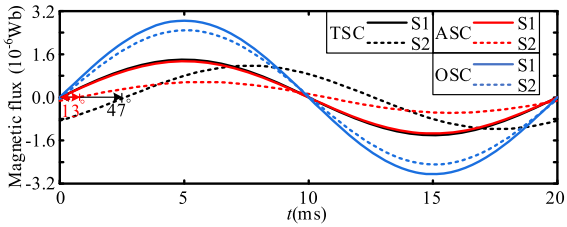

Fig. 15. Simulation results in magnetic flux at different core cross sections (S1, S2) when $I_P = 100$ A.

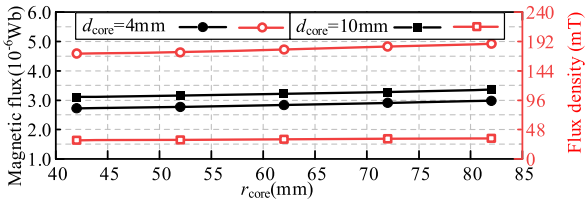

Fig. 16. Simulation results of the magnetic flux and magnetic flux density of the core column as a function of r_{core} when $I_P = 100$ A.

TABLE III
EFFECT OF CORE COLUMN LENGTH ON FLUX AND FLUX DENSITY

\	\	Initial value	Final value	Percentage
$d_{core} = 10$ (mm)	Magnetic flux (10^{-6} Wb)	3.11	3.36	+8.04%
	Flux density (mT)	30.37	33.59	+10.6%
$d_{core} = 4$ (mm)	Magnetic flux (10^{-6} Wb)	2.72	2.98	+9.56%
	Flux density (mT)	172.32	188.34	+9.3%

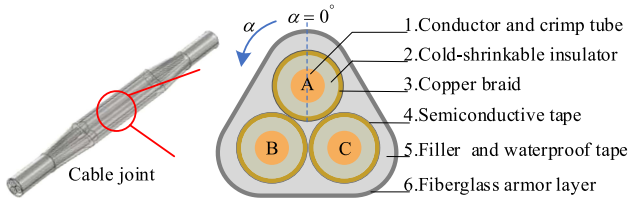

Fig. 17. Schematic diagram of three-core cable joint [23].

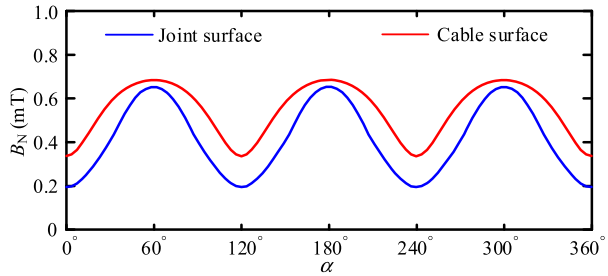

Fig. 18. Simulation results of the surface B_N amplitude for cable and cable joint at $I_P = 100$ A.

effect of the magnetic fluxes of phases B and C on the induced voltage. Besides, there is a phase deviation of the magnetic flux at different locations, which reduces the vector sum of the induced voltage of the N-turn coil. In comparison, ASC reduces the weakening effect of the other two Phase magnetic fluxes by shortening the length of the magnetic core that surrounds the cable. As a result, the phase difference of the flux decreases. However, there is a significant reduction in the flux value near the ends of the core due to the demagnetizing effect. The magnetic flux of OSC is approximately twice that of the previous two core types. The flux phase and amplitude at different locations are also highly consistent. These findings effectively demonstrate the superiority of the proposed magnetic coupler.

To verify the influence of OS-MFEH core column length l on $\mu_{eff,\,eq}$, Fig. 16 shows the simulation results for the magnetic flux passing through the cross-section S1 and the flux density at point P_C [P_C shown in Fig. 7(b)] as a function of the core column radius r_{core}. When core column radius r_{core} increases from 42 to 82 mm, l rises by 154.43% (from 106 to 269.7 mm). By contrast, the growth of magnetic flux and flux density remains minimal. The specific comparison results are shown in Table III. Magnetic flux and flux density are directly proportional to $\mu_{eff,eq}$. Therefore, when the distance between the two ends of the core column is fixed, extending l cannot effectively increase $\mu_{eff,eq}$. r_{core} does not need to be too large, which is meaningful for reducing core material consumption and shrinking the size of the energy harvester. On the other hand, the effect of varying d_{core} on magnetic flux and flux density is significant, as shown in Fig. 16. So, optimizing d_{core} is crucial.

Fig. 17 shows a schematic diagram of a three-core cable joint. The relative permeability of each layer of material in the cable joint is approximately 1, thus providing no magnetic shielding effect [23]. To verify the feasibility of applying OS-MFEH in a three-core cable joint scenario, Maxwell simulation was used to measure the magnitude of the normal magnetic flux density BN around the cable joint surface. The results are shown in Fig. 18. The location of the BN maximum value distribution aligns with the cable body. Therefore, the proposed energy harvester structure is equally applicable to the cable joint.

B. Experimental Prototype Setup

To verify the analysis, an experimental platform is built, as shown in Fig. 19. The cable has a rated current-carrying capacity of 255 A in air. The experimental equipment information is given in Table IV. Four OS-MFEH prototypes are fabricated,

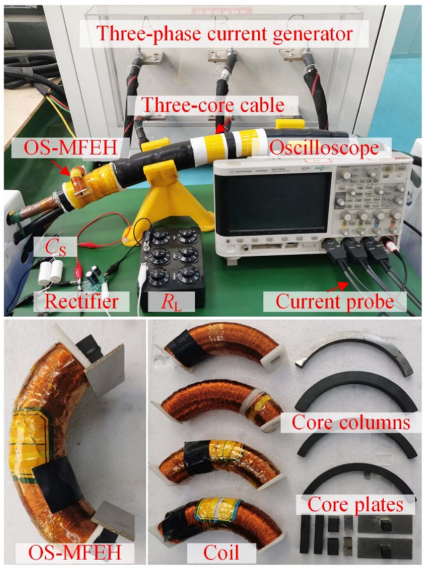

Fig. 19. Experimental platform configuration.

TABLE IV
MODEL AND MANUFACTURER OF LABORATORY EQUIPMENT

Equipments	Models	Producers
High-current generator	GSSAQ-1500SW	Wuhan Guoshi
Oscilloscope	DSO-X 3034A	Agilent
Current probe	N2780B	Agilent
Voltage probe	DP-25	Deken
Multimeter	17B+	Fluke
Rectifier diode	SVM1060X R1	PANJIT

TABLE V
PARAMETERS OF THE EXPERIMENTAL PROTOTYPES

\	d_w(mm)	d_{core}(mm)	N/exp.	N/cal.	R_{wire}(Ω)/exp.
OS-MFEH1	0.2	6	6600	8200	170
OS-MFEH2	0.2	8	5500	6900	153.2
OS-MFEH3	0.1	6	25000	30000	2842
OS-MFEH4	0.1	8	18000	25300	2408

TABLE VI
PARAMETERS OF THE CORE MATERIALS

Properties	Ferrite PC95	Permalloy 1J85	Fe-Si Steel B30P100
Relative permeability μ_r	3300	40000	4000
Electrical resistivity(Ω·m)	6	5.6×10^{-7}	4.7×10^{-7}
Saturation magnetic flux density B_{sat}(T)	0.5	0.7	2

as given in Table V. Owing to hand-winding errors, the actual number of turns in the experiment deviates from the theoretical values, and the subsequent calculations are based on the measured data. Table VI lists the core material properties. To reduce eddy current loss, the core column of the B30P100 Fe-Si steel is manufactured by laminating 0.3 mm-thick sheets. Due to processing difficulties, the core column of the 1J85 permalloy can only be made by laminating 1 mm plates.

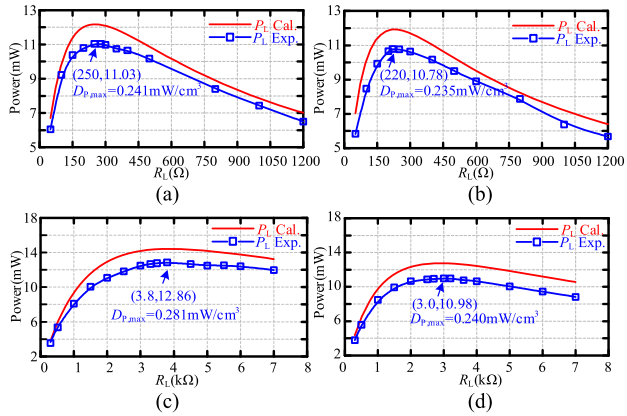

Fig. 20. Theoretical calculations and experimental results of P_L versus R_L for cores made of PC95 ferrite. (a) OS-MFEH1. (b) OS-MFEH2. (c) OS-MFEH3. (d) OS-MFEH4.

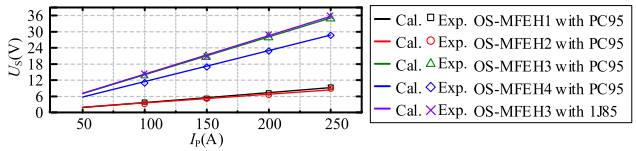

Fig. 21. Theoretical calculations and experimental results of U_S as a function of I_P.

C. Experimental Results

Fig. 20 illustrates theoretical calculations and experimental results of P_L versus R_L when I_P is 100 A, for different values of d_{core} and d_w. As the same d_w, the maximum power of the harvesters with $d_{core} = 8$ mm and $d_{core} = 6$ mm shows little difference. Besides, for the same d_{core}, the harvester with $d_w = 0.1$ mm exhibits a higher output power than that with $d_w = 0.2$ mm. Moreover, the former offers an advantage in the selection of power management converters owing to its higher load voltage. The optimized OS-MFEH3 achieves a maximum power of 12.86 mW with a power density of 0.281 mW/cm^3. The phenomena above are consistent with the analyses in Section IV. The maximum error between the experimental values and the theoretical values of P_L is 8.24% based on (22). Fig. 21 shows the theoretical calculations and experimental results for U_S as a function of I_P. In Fig. 21, the error between the calculated value and the measured value of U_S is about 5% based on (21). On the one hand, it suggests that part of the measurement error in power stems from system loss under load (e.g., eddy current loss). On the other hand, this indicates that an external magnetic field alone is insufficient to saturate the magnetic core.

Fig. 22 presents the output power curves of the OS-MFEH1 as a function of load under three core materials at $I_P = 250$ A. Under the parameters of OS-MFEH1, μ_r values of the three materials sufficiently meet $\mu_{r,th}$, which means that effective permeability $\mu_{eff,eq}$ of cores made from these three materials is identical. Thus, according to (22), the theoretical curves of energy harvesters using these three core materials show negligible differences when the core is unsaturated. However, it is worth noting that for the PC95 and 1J85 materials, the measured power deviates significantly from the theoretical value in the

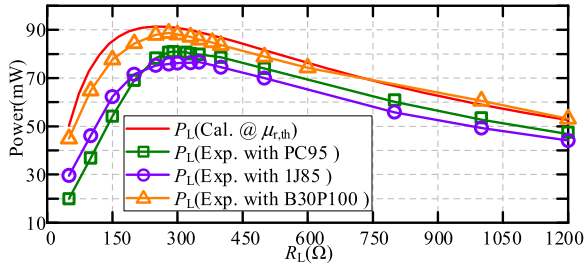

Fig. 22. Theoretical calculations and experimental results of P_L versus R_L for OS-MFEH1 with different materials.

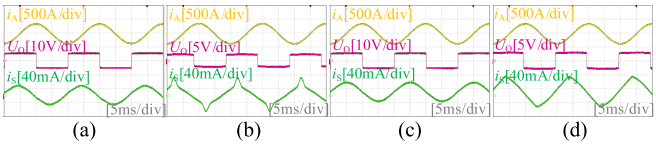

Fig. 23. Experimental waveforms under different load and materials conditions. (a) $R_L = 300\ \Omega$, PC95. (b) $R_L = 100\ \Omega$, PC95. (c) $R_L = 300\ \Omega$, 1J85. (d) $R_L = 100\ \Omega$, 1J85.

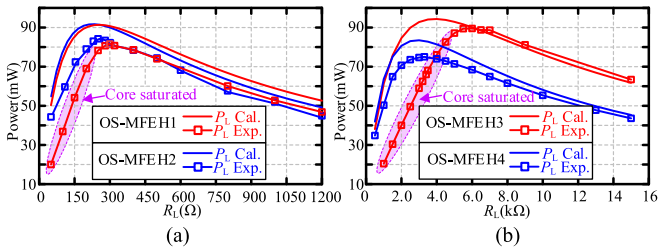

Fig. 24. Theoretical calculations and experimental results of P_L versus R_L for the OS-MFEHs with different d_{core} when I_P is 250 A and the core material is PC95. (a) $d_w = 0.2$ mm. (b) $d_w = 0.1$ mm.

range where R_L is less than 200 Ω. In particular, at $R_L = 50\ \Omega$, the measured power of the OS-MFEH with PC95 is only 40% of the theoretical value, which can be attributed to core saturation. Consequently, P_L decreases as $\mu_{eff,eq}$ decreases. Furthermore, since the resistivity of 1J85 is lower than that of PC95, the eddy current loss is higher. Therefore, when R_L exceeds 300 Ω, P_L of the former is lower than that of the latter. Compared with the previous two materials, OS-MFEH1 with B30P100 exhibits higher saturation magnetic flux density B_{sat} and lower eddy current loss. As a result, the experimental values are close to the theoretical values across the entire R_L variation range.

Fig. 23 shows the measured waveforms of OS-MFEH1 under different loads with two core materials at $I_P = 250$ A. At $R_L = 300\ \Omega$, I_S is a complete sine wave. Due to the complete resonance between C_S and L_S, the entire system exhibits a purely resistive characteristic. At $R_L = 100\ \Omega$, the core saturates, I_S becomes distorted, L_S decreases. According to (31), when $R_L = 100\ \Omega$, $B_{all} = 0.63$ T, this value exceeds B_{sat} of PC95. The above phenomena indicate that the magnetic field generated by I_S exerts a significant impact on the operating state of the core.

As analyzed in Section IV, the core column with the larger d_{core} values exhibits stronger anti-saturation capabilities. Fig. 24 presents the output power curves of the OS-MFEHs with different d_{core} as a function of load. As shown in Fig. 24(a), when R_L is less than 300 Ω, the power harvesting capability of OS-MFEH2 is significantly improved compared to OS-MFEH1.

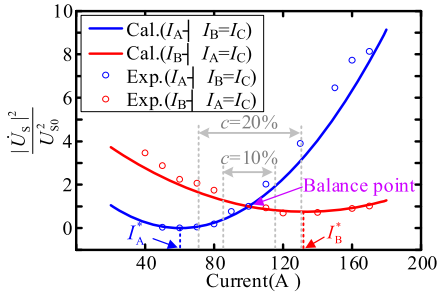

Fig. 25. Theoretical calculations and experimental results of the ratio of the square of the unbalanced induced voltage magnitude to that of the balanced induced voltage U_{S0}^2.

For example, at $R_L = 150\ \Omega$, the former achieves a power output of 72.4 mW, while the latter yields 54.15 mW, corresponding to a 1.34-fold increase. Furthermore, at $R_L = 250\ \Omega$, OS-MFEH2 achieves 84.2 mW of power. Similarly, the results in Fig. 24(b) indicate that the OS-MFEH4 with $d_{core} = 8$ mm does not saturate; consequently, experimental values are close to theoretical values over the entire load range, with the maximum error being 10% . Therefore, for core material with $B_{sat} < B_{all}$, slightly increasing d_{core} effectively prevents core saturation.

To verify the output of OS-MFEH under current imbalance conditions, the induced voltage was tested under the following two scenarios.

1) Phase A current imbalance ($I_A \neq I_B = I_C$).
2) Phase B current imbalance ($I_B \neq I_A = I_C$).

The test prototype selected for OS-MFEH3 ($M_A = 1123.56\ \mu$H, $M_B = M_C = 679.41\ \mu$H) with a 100 A current reference. The ratio of the square of the unbalanced induced voltage magnitude to that of the balanced induced voltage $U2$ S0 is presented in Fig. 25. Within the range of three-phase current imbalance ($c < 20\%$), the voltage increases relative to its balanced-state value when I_A rises (or I_B falls). However, when $c > 20\%$ and $I_A < I_A^* = 60.47$ A, the induced voltage generated by I_A will be lower than that generated by I_B and I_C. Thus, the total induced voltage increases instead as I_A decreases. For $I_B > I_B^* = 132.69$ A, the induced voltage generated by I_B becomes dominant as I_B increases, leading to a rise in the total induced voltage with increasing I_B. However, under normal circumstances, c does not exceed 10% [22]. Within this range, the induced voltage increases to a maximum of 1.41 times that in the balanced state (19.61 V) and decreases to a minimum of 62.1% of that in the balanced state (8.66 V). In conclusion, OSC-MFEH can still supply power to the load even when three-phase current imbalance occurs. When a short-circuit fault occurs in the cable, the massive unbalanced current causes voltage spikes in the OS-MFEH. Therefore, it is necessary to add protective measures at the OS-MFEH output, such as a transient voltage suppressor.

D. Comparison

Table VII lists the comparisons between previous studies and this article. The OSC solves the inherent contradiction of the fully surrounded structures (toroidal core and three split cores) [13], [14], [16]: close installation compresses the coil space,

TABLE VII
COMPARISON OF THIS ARTICLE WITH PREVIOUS STUDIES

	[13]	[14]	[15]	[16]	[17]	[18]	This article
Cable radius	26.5 mm	26.5 mm	30 mm	26.5 mm	16.7 mm	35.25 mm	32 mm
Core structure	Toroidal core	Toroidal core	Three-slot/three-tooth core	Three-split cores	Notched ring core	Three-slot/three-tooth core	Omega-shaped core
Cable current	300 A_{RMS}	125 A_{AMP}	50 A_{RMS}	200 A_{AMP}	100 A_{AMP}	100 A_{RMS}	100 A_{RMS}
Induced voltage	1 V_{AMP}	248.3 mV_{AMP}	0.55 V_{RMS}	400 mV_{AMP}	16.6 V_{AMP}	2.5 V_{AMP}	13.5 V_{RMS}
Output power	8.16 μW	\	2.243 mW	\	28.4 mW	105 mW	12.86 mW
Volume	\	120 cm^3	465 cm^3	73.5 cm^3	\	about 1734 cm^3	45.6 cm^3
Power density	\	\	4.82 $\mu W/cm^3$	\	\	0.061 mW/cm^3	0.281 mW/cm^3
Design method	FEA	FEA	FEA and NNA	FEA	FEA	FEA	Mathematical calculation

while distant placement weakens the magnetic field coupling. Compared to [17], both the OSC and the notched ring core effectively shorten the length of the coupling air gap magnetic circuit between the coil and the current-carrying conductor, thereby reducing magnetic field energy loss. However, OS-MFEH offers higher space utilization. This is because the core radius of the OSC is almost independent of the effective permeability, which means that OS-MFEH can be designed to be very compact. Furthermore, the adoption of core plates increases magnetic flux and improves effective permeability. Compared with [15] and [18], the OS-MFEH achieves high power density with less core material. After normalized current excitation, the power density of OS-MFEH increased by 14.57 times and 4.6 times compared with [15] and [18], respectively. More significantly, this design method differs greatly from the finite-element analysis (FEA) and neural network algorithms (NNAs) commonly used in previous studies [15], [17], [18]. This article is based on a theoretical model to optimize the core and coil parameters, greatly reducing the complexity and time required for MFEH design.

VI. CONCLUSION

This article proposes a MFEH with the OSC. By reconfiguring the magnetic circuit of the core at the two points of maximum normal magnetic flux density on the surface of the three-core cable, the phase of the composite magnetic flux entering the core is made consistent with the phase of the target conductor current. This reduces the weakening of the induced voltage caused by the flux of the other two Phases. Besides, the established mathematical model not only guides the optimization of the OS-MFEH's core and coil parameters but also determines the critical current and load at which the core saturates. Considering the coil magnetic field, materials with higher saturation magnetic flux density are required for the core. Compared to ferrites and permalloy commonly used in previous studies, silicon steel with a high saturation magnetic flux density is more suitable. Additionally, increasing the core column side length can effectively prevent core saturation. It can also mitigate the impact of fluctuations in effective permeability caused by changes in relative permeability. The optimized OS-MFEH volume is 45.8 cm^3 and can achieve an output power of 12.86 mW to 84.2 mW within a cable current range of 100 A_{RMS} to 250 A_{RMS}. Within a three-phase current imbalance of 10% , OS-MFEH can still supply power to the load.

For future research, we will fully leverage the flexible magnetic metals to develop a universal magnetic core structure and coil solution suitable for different cable models and cable joints. The magnetic armoring layer significantly shields the magnetic field that MFEHs can harvest, and this limitation will be the focus of our subsequent research efforts. Moreover, we will explore MPPT algorithms tailored to the OS-MFEH's output features—specifically, addressing the dynamic adjustment needs arising from fluctuations in cable current. We will also integrate the load characteristics of typical sensors (e.g., low power consumption, intermittent operation) to optimize the MPPT control strategy.

APPENDIX

This section provides supplementary derivations for some of the formulas in the main text.

$A_T(\alpha)$ and $A_N(\alpha)$ in (2) are obtained from (34)

$$\begin{cases} A_T(\alpha) = \frac{\sqrt{2}\mu_0 I_P}{2\pi} \cdot \frac{\sqrt{X_T^2+Y_T^2+2X_TY_T\cos(3\alpha)}}{W} \\ A_N(\alpha) = \frac{\sqrt{2}\mu_0 I_P}{2\pi} \cdot \frac{\sqrt{X_N^2+Y_N^2+2X_NY_N\cos(3\alpha)}}{W} \end{cases}. \tag{34}$$

Meanwhile, $\varphi_T(\alpha)$ and $\varphi_N(\alpha)$ are calculated by (35)

$$\begin{cases} \varphi_T(\alpha) = \arctan\left[\frac{X_T\sin(-\alpha)+Y_T\sin(2\alpha)}{X_T\cos(-\alpha)+Y_T\cos(2\alpha)}\right] \\ \varphi_N(\alpha) = \arctan\left[\frac{X_N\sin(-\alpha)+Y_N\sin(2\alpha)}{X_N\cos(-\alpha)+Y_N\cos(2\alpha)}\right] \end{cases}. \tag{35}$$

The coefficients in (34) and (35) are expressed as

$$\begin{cases} X_T = 3s(r^4-s^4), \quad Y_T = 3rs^2(r^2-s^2) \\ X_N = 3s(r^4+s^4), \quad Y_N = -3rs^2(r^2+s^2) \\ W = 2\left[r^6 - 2r^3s^3\cos(3\alpha) + s^6\right] \end{cases}. \tag{36}$$

REFERENCES

[1] Y. Wu and P. Zhang, "A novel online monitoring scheme for underground power cable insulation based on common-mode leakage current measurement," *IEEE Trans. Ind. Electron.*, vol. 69, no. 12, pp. 13586–13596, Dec. 2022, doi: 10.1109/TIE.2022.3142434.

[2] Y. Wu, Y. Yang, Z. Wang, and P. Zhang, "Online monitoring for underground power cable insulation based on common-mode signal injection," *IEEE Trans. Ind. Electron.*, vol. 69, no. 7, pp. 7360–7371, Jul. 2022, doi: 10.1109/TIE.2021.3102410.

[3] Y. Li, N. Duan, Z. Liu, J. Hu, and Z. He, "Impedance-matching-based maximum power tracking for magnetic field energy harvesters using active rectifiers," *IEEE Trans. Ind. Electron.*, vol. 70, no. 10, pp. 10730–10739, Oct. 2023, doi: 10.1109/TIE.2022.3219064.

[4] Z. Liu, Y. Li, H. Yang, N. Duan, and Z. He, "An accurate model of magnetic energy harvester in the saturated region for harvesting maximum power: Analysis, design, and experimental verification," *IEEE Trans. Ind. Electron.*, vol. 70, no. 1, pp. 276–285, Jan. 2023, doi: 10.1109/TIE.2022.3156033.

[5] H. Xiao, H. Peng, Y. Zhao, and L. Hou, "Magnetic field energy harvesting and power management with transfer window modulation," *IEEE Trans. Power Electron.*, vol. 40, no. 5, pp. 7573–7585, May 2025, doi: 10.1109/TPEL.2025.3528110.

[6] S. Yuan, Y. Huang, J. Zhou, Q. Xu, C. Song, and P. Thompson, "Magnetic field energy harvesting under overhead power lines," *IEEE Trans. Power Electron.*, vol. 30, no. 11, pp. 6191–6202, Nov. 2015, doi: 10.1109/TPEL.2015.2436702.

[7] S. Yuan, Y. Huang, J. Zhou, Q. Xu, C. Song, and G. Yuan, "A high-efficiency helical core for magnetic field energy harvesting," *IEEE Trans. Power Electron.*, vol. 32, no. 7, pp. 5365–5376, Jul. 2017, doi: 10.1109/TPEL.2016.2610323.

[8] H. Yang, Y. Li, Z. Liu, H. Luo, Y. Yan, and Z. He, "An accurate power model and high power density design method of free-standing magnetic field energy harvesters with H-shaped core," *IEEE Trans. Ind. Electron.*, vol. 70, no. 8, pp. 7965–7975, Aug. 2023, doi: 10.1109/TIE.2022.3225854.

[9] H. Yang, Y. Li, Y. Yan, H. Luo, and Z. He, "A magnetic flux collection enhanced arc-shaped core and its optimal coil turn design method of free-standing magnetic field energy harvester," *IEEE Trans. Power Electron.*, vol. 38, no. 11, pp. 13567–13572, Nov. 2023, doi: 10.1109/TPEL.2023.3301505.

[10] Z. Liu et al., "Mathematical modeling and optimization for the power density of the free-standing magnetic field energy harvester," *IEEE Trans. Power Electron.*, vol. 39, no. 5, pp. 6421–6432, May 2024, doi: 10.1109/TPEL.2024.3369749.

[11] Z. Liu et al., "Harmonic magnetic field energy harvesting for self-powered sensors in HVDC transmission lines," *IEEE Trans. Power Electron.*, vol. 40, no. 3, pp. 4536–4545, Mar. 2025, doi: 10.1109/TPEL.2024.3508091.

[12] S. M. Gargari, P. A. A. F. Wouters, P. C. J. M. van der Wielen, and E. F.Steennis, "Partial discharge parameters to evaluate the insulation condition of online located defects in medium voltage cable networks," *IEEE Trans.Dielect. Elect. Insul.*, vol. 18, no. 3, pp. 868–877, Jun. 2011, doi: 10.1109/TDEI.2011.5931076.

[13] Q. Feng et al., "Design and optimization of the energy harvesting device for wireless sensors," in *Proc. IEEE 4th Int. Conf. Electr. Mater. Power Equip.*, 2023, Art. no. 10138939.

[14] B. Nan, X. Lu, T. Sun, Y. Lin, H. Li, and J. Li, "Development of thermal condition evaluation system based on energy self-harvesting technique for three-core power cables," *Smart Power*, vol. 48, no. 11, pp. 103–107, Nov. 2020.

[15] P. Yan et al., "Research on the high-efficient coupling energy self-harvesting from three-phase rotating magnetic field," *Chin. J. Sci. Instrum.*, vol. 45, no. 6, pp. 288–296, Jun. 2024.

[16] T. X. Sun, X. F. Zeng, Y. X. Lu, and H. J. Li, "Research on energy harvesting and its application in thermal condition monitoring of three-core power cables," in *Proc. 21st Int. Symp. High Voltage Eng.*, 2020, vol. 598, pp. 684–696.

[17] L. Liu, X. Wen, R. Shi, P. Li, Y. Wen, and T. Han, "High-efficiency magnetic field energy harvesting from a three-core cable," *Sens. Actuators A Phys.*, vol. 360, Oct. 2023, Art. no. 114501.

[18] T. Zhan, J. Wei, B. Zhao, G. Yang, H. Gan, and X. Zeng, "Research on energy harvesting device of 10 kV three-core cable based on self-collecting energy," in *Proc. 14th Int. Conf. Power Energy Syst.*, 2024, pp. 218–222.

[19] H. Yang et al., "Efficiency analysis and optimization method of power-relay IPT systems for reefer containers," *IEEE Trans. Power Electron.*, vol. 36, no. 5, pp. 4942–4947, May 2021, doi: 10.1109/TPEL.2020.3030902.

[20] M. Wang, J. Feng, Y. Shi, and M. Shen, "Demagnetization weakening and magnetic field concentration with ferrite core characterization for efficient wireless power transfer," *IEEE Trans. Ind. Electron.*, vol. 66, no. 3, pp. 1842–1851, Mar. 2019, doi: 10.1109/TIE.2018.2840485.

[21] P. Martín-Luna et al., "On the magnetic field of a finite solenoid," *IEEE Trans. Magn.*, vol. 59, no. 4, Apr. 2023, Art. no. 7000106, doi: 10.1109/TMAG.2023.3250837.

[22] K. Zhu, W. K. Lee, and P. W. T. Pong, "Energization - status identification of three-phase three-core shielded distribution power cables based on non-destructive magnetic field sensing," *IEEE Sensors J*, vol. 17, no. 22, pp. 7405–7417, Nov. 2017, doi: 10.1109/JSEN.2017.2756905.

[23] L. Chen, R. Niu, and H. Zhou, "Research of the inverse relationship between internal and external temperatures of 10 kV three-core cable joints," *IEEE Access*, vol. 12, pp. 167236–167244, 2024, doi: 10.1109/ACCESS.2024.3496541.

Yonghong Zhou received the B.Sc. degree in electrical engineering from the School of Electrical Engineering, Qingdao University, Qingdao, China, in 2023. He is currently working toward the M.Sc. degree in electrical engineering with the School of Electrical Engineering, Southwest Jiaotong University, Chengdu, China.

His primary research focus is magnetic field energy harvesting, particularly enhancing the power density of free-standing magnetic field energy harvesters.

Yong Li (Senior Member, IEEE) received the B.Sc. and Ph.D. degrees in electrical engineering from the School of Electrical Engineering, Southwest Jiaotong University, Chengdu, China, in 2013 and 2017, respectively.

From 2017 to 2018, he was a Research Associate with the Department of Electrical Engineering, The Hong Kong Polytechnic University, and subsequently, he was a Post-Doctoral Fellow with the same department. He is currently an Associate Professor with Southwest Jiaotong University, Chengdu, China. He is a Guest Editor of electronics for a special issue "Wireless Power Transfer and Its Applications." His main research interests are wireless power transfer and energy harvesting.

Shunpan Liu (Senior Member, IEEE) received B.Sc. and Ph.D. degrees in electrical engineering from Southwest Jiaotong University, Chengdu, China, in 2018 and 2023, respectively.

He is currently a Postdoctoral Researcher with Southwest Jiaotong University. His main research interest focuses on wireless power transfer, especially on Modelling and control methods of dynamic wireless power transfer system.

Jiefeng Hu (Senior Member, IEEE) received the Ph.D. degree in electrical engineering from the University of Technology Sydney, Ultimo NSW, Australia, in 2013.

He was involved in the research of minigrids with the Commonwealth Scientific and Industrial Research Organization. He was an Assistant Professor with Hong Kong Polytechnic University, Hong Kong. He is currently an Associate Professor with Federation University Australia.

Dr. Hu is an Editor for IEEE TRANSACTIONS ON ENERGY CONVERSION, and a Guest Editor for IEEE TRANSACTIONS ON INDUSTRIAL ELECTRONICS for a special issue "Applications of Predictive Control in Microgrids." His research interests include power electronics, renewable energy, and smart microgrids.

Zhengyou He (Senior Member, IEEE) received the B.Sc. and M. Sc. degrees in computational mechanics from Chongqing University, Chongqing, China, in 1992 and 1995, respectively, and the Ph.D. degree in electrical engineering from the School of Electrical Engineering from Southwest Jiaotong University, Chengdu, China, in 2001.

He is currently a Professor with the School of Electrical Engineering, Southwest Jiaotong University. His research interests include signal process and information theory applied to electrical power system, and application of wavelet transforms in power systems.